Research Article

OPTICA QUANTUM

Fast and reliable atom transport by optical tweezers

Sunhwa Hwang,[1] Hansub Hwang,[1] Kangjin Kim,[1] Andrew Byun,[1] Kangheun Kim,[1] Seokho Jeong,[1] Maynardo Pratama Soegianto,[1,2] and Jaewook Ahn[1,*]

[1]Department of Physics, KAIST, Daejeon 34141, Republic of Korea
[2]Department of Physics, Institut Teknologi Bandung, Jawa Barat 40132, Indonesia
*jwahn@kaist.ac.kr

Received 4 November 2024; revised 7 January 2025; accepted 8 January 2025; published 30 January 2025

Movable single atoms have drawn significant attention for their potential as flying quantum memory in non-local, dynamic quantum computing architectures. However, when dynamic optical tweezers are employed to control atoms opto-mechanically, conventional methods such as adiabatic controls and constant jerk controls are either inherently slow or induce mechanical heating, leading to atom loss over long distances or at high speeds. To address these challenges, we explore the method known as shortcuts to adiabaticity (STA) as an efficient alternative for fast and reliable atom transport. We present a series of proof-of-concept experiments demonstrating that STA-based optical tweezer trajectories can achieve both rapid and reliable single-atom transport. These experiments include moving atoms between two locations, adjusting speeds en route, and navigating curved trajectories. Our results indicate that atoms can be transported with a constant acceleration on average over distances that is only limited by trap lifetime, while effectively suppressing vibrational heating. This makes STA methods particularly well-suited for long-distance atom transport, potentially spanning distances over centimeter scales, such as between quantum information devices.

https://doi.org/10.1364/OPTICAQ.546797

1. INTRODUCTION

There is a growing interest in neutral-atom quantum computing research [1–8], largely due to the scaling potential of these systems, as demonstrated by their ability to trap thousands of atoms as individual qubits [9,10]. At the same time, a significant challenge is emerging around effectively controlling and, in particular, moving these atoms spatially. As neutral-atom quantum devices are expected to partition space into distinct zones for operations such as entanglement, storage, and readout, atoms are to be transferred between these zones [5–7]. As the system size increases, meaning the number of atoms and the area they occupy expand, the distance and time required for these transfers will also grow, raising the risk of disrupting their internal states.

The traditional approach is the “adiabatic" process [11–13], which preserves the quantum state by slowly evolving the system along the instantaneous eigenstates of a time-dependent Hamiltonian. Efficient atom transport within quantum information devices, traditionally requiring substantial time to prevent heating and preserve quantum states, has become increasingly important [14–17]. However, accelerating this process introduces side effects, referred to as the “diabatic" process [13,18–20]. Despite its effectiveness in maintaining the system’s internal state, the inherent slowness of adiabatic operations can pose challenges when faced with practical time constraints in quantum computing operations. In this context, while the constant jerk trajectory [5,14] is considered as an alternative approach to minimize the average kinetic energy of atoms during transport, this method does not fully prevent the heating of the atoms during the transport process [5].

The method of the shortcuts to adiabaticity (STA) in quantum mechanics offers a faster alternative to the adiabatic process, achieving the same outcomes of adiabatic processes without typical time constraints, making them suitable for time-sensitive scenarios [13,21–24]. We focus on fast and reliable single-atom transport by controlling optical tweezers along STA-based trajectories. Optical tweezers [25–28] have been useful for manipulation of single atoms, which is essential for reconfiguring atom arrays [29–33] and facilitating qubit entanglements [34,35] in neutral atom quantum computing. In this paper, we will first verify the effectiveness of the STA method in an optical tweezer system and define its experimental limits. We will then conduct experiments to evaluate its applicability for generalized curved trajectories, in contrast to simple straight paths. Finally, we will discuss the potential advantages of this approach for long-distance transport, comparing it with other transportation methods.

2. SHORTCUTS-TO-ADIABATICITY TRAJECTORY

We design an optical tweezer path $x_o(t)$ to implement STA-based atom transport along $x(t)$ using the invariant-based inverse engineering technique [13,14]. The optical tweezer’s potential is approximated as a truncated harmonic potential [20,27], given

by

$$U(x,t) = \frac{U_0}{d^2}[x - x_o(t) - d][x - x_o(t) + d], \quad (1)$$

where U_0 is the optical potential depth, d is the width of the optical tweezer, $\omega_0 = \sqrt{2U_0/md^2}$ is the trap frequency, and m the atom mass. The atom's dynamics is then governed by

$$\ddot{x} + \omega_0^2[x - x_o(t)] = 0 \quad \text{for} \quad |x - x_o(t)| < d. \quad (2)$$

Using this harmonic approximation, the appropriate atom path that ensures its final state matches its initial state is described by (in scaled position and time, $\tilde{x} = x/l$ and $\tilde{t} = t/t_f$)

$$x(t) = v_i t + (10l - 6v_i t_f - 4v_f t_f)\tilde{t}^3 - (15l - 8v_i t_f - 7v_f t_f)\tilde{t}^4 + (6l - 3v_i t_f - 3v_f t_f)\tilde{t}^5, \quad (3)$$

using a polynomial ansatz to satisfy the boundary conditions,

$$x(0) = 0,\ \dot{x}(0) = v_i, \quad \ddot{x}(0) = 0, \quad (4a)$$

$$x(t_f) = l, \dot{x}(t_f) = v_f, \ddot{x}(t_f) = 0, \quad (4b)$$

to transport the atom from $x = 0$ to $x = l$ over the time interval from $t = 0$ to $t = t_f$. The optical tweezer trajectory, $x_o(t)$, facilitating the atom transport path in Eq. (3), is then obtained from the equation of motion in Eq. (2). For the specific case where the atom's initial and final velocities are both zero, $v_i = v_f = 0$, the atom and optical tweezer trajectories are simplified as follows:

$$\tilde{x}(t) = 10\tilde{t}^3 - 15\tilde{t}^4 + 6\tilde{t}^5, \quad (5)$$

$$\tilde{x}_o(t) = \tilde{x}(t) + \frac{60}{\omega_0^2 t_f^2}\tilde{t} - \frac{180}{\omega_0^2 t_f^2}\tilde{t}^2 + \frac{120}{\omega_0^2 t_f^2}\tilde{t}^3. \quad (6)$$

Furthermore, two-dimensional (2D) scenarios, such as rotational paths with a fixed radius R, can be addressed using the inverse engineering method [36]. Solutions for curved paths in two dimensions can serve as a basis for designing more complex, multi-shaped paths. Unlike the computationally challenging general solution [36], STA-based solutions for rotating atomic transport can be classically simplified in polar coordinates ($\tilde{\theta} = \theta/\theta_f$ and $\tilde{t} = t/t_f$), by leveraging the radial symmetry of the optical tweezers, as follows:

$$\theta(t) = \left(\frac{v_i t_f}{R}\right)\tilde{t} - \left(\frac{6v_i t_f + 4v_f t_f}{R} - 10\theta_f\right)\tilde{t}^3 + \left(\frac{8v_i t_f + 7v_f t_f}{R} - 15\theta_f\right)\tilde{t}^4 - \left(\frac{3v_i t_f + 3v_f t_f}{R} - 6\theta_f\right)\tilde{t}^5. \quad (7)$$

These simplified solutions need to satisfy the boundary conditions

$$\theta(0) = \theta_o(0) = 0, \quad \dot{\theta}(0) = v_i/R, \quad (8a)$$

$$\theta(t_f) = \theta_o(t_f) = \theta_f, \quad \dot{\theta}(t_f) = v_f/R. \quad (8b)$$

3. STA-BASED SINGLE-ATOM TRANSPORT

Our experiments utilize a 2D atom array system described previously [8,20,30–32]. Laser-cooled rubidium atoms (^{87}Rb) were trapped in static optical tweezers generated by a 2D spatial light modulator (ODPDM-512 by Meadowlark Optics) and manipulated with dynamic optical tweezers controlled by a pair of acousto-optic deflectors (AOD) (DTSXY-400-820 by AA Opto Electronics) and arbitrary waveform generators (AWG, M4i-6622-x8 by Spectrum Instrumentation and OPX+ by Quantum Machines). Both the static and dynamic optical tweezers were operated with a wavelength of 820 nm and a trap frequency of $\omega_0 = \sqrt{2U_0/md^2} = 2\pi \times 90(10)$ kHz, where $U_0 = 0.8(2)$ mK is the optical potential depth, m is the atom mass, and $d = 0.73(7)$ μm is the harmonic-trap width [20]. Atom detection was performed using fluorescence imaging of the $5S_{1/2}$–$5P_{3/2}$ transition, with an objective lens that had a numerical aperture of 0.5.

Figure 1 illustrates the reliable performance of STA-based atom transport following Eq. (5) compared with the non-STA, CV method ("adiabatic solution" in the adiabatic region). To calculate the change of the atomic energy distribution, we modeled the initial distribution of atoms in an optical tweezer using the Maxwell–Boltzmann distribution and the quantum harmonic oscillator model, and numerically calculates the evolution of their motion and distribution over time using the fourth-order Runge-Kutta method. Based on this simulation, we can calculate the vibrational state n distribution and the changes in atomic wave packets during the STA and non-STA transport, which are shown in Figs. 1(a) and 1(b), respectively, with transport conditions set as a distance of $l = 12.6(3)$ μm, duration of $t_f = 58.5(8)$ μs, and initial atomic temperature of 27(3) μK for both simulations. The STA transport in Fig. 1(a) is based on Eqs. (5) and (6), successfully maintaining the initial atom conditions. The non-STA trajectory in Fig. 1(b) is a constant velocity trajectory with the same average speed employed in a diabatic region, where the transport condition induces diabatic processes, i.e., $\Delta n \ll 1$, with $|n\rangle$ representing vibrational energy state. While, at sufficiently slow transport speeds within an adiabatic region ($\Delta n \ll 1$), atoms following this uniform linear trajectory could maintain their initial conditions, such as vibrational energy states and temperature, moving the atom along the non-STA trajectory given in the diabatic region results in failure or deformation of the atom's initial state population, as shown in Fig. 1(b).

In order to measure the energy distribution of the atoms in the optical tweezer, we use the adiabatic trap lowering method [28]. It involves three steps: (i) slowly decreasing the trap depth to a minimum value, $U_{\min}$; (ii) holding the trap depth at $U_{\min}$ for a sufficient duration; and (iii) slowly increasing the trap depth back to its initial value, U_i. During the first and last steps, the gradual adjustment of the trap depth ensures an adiabatic process, preserving the vibrational mode of the atoms. At the minimum trap depth, atoms with energy higher than the cutoff energy E_c (corresponding to $U_{\min}$) escape, leaving behind atoms with energy lower than E_c. This process allows for the determination of the cumulative probability distribution of atomic energy by measuring the survival probability of atoms. If the atoms follow the Maxwell–Boltzmann distribution, the cumulative probability distribution function is given by

$$P(E_c) = \int_0^{E_c} f_{\mathrm{MB}}(E')\,\mathrm{d}E' = 1 - \left[1 + \eta + \frac{\eta^2}{2}\right]e^{-\eta}, \quad (9)$$

where f_{MB} is the normalized Maxwell–Boltzmann energy distribution function for atoms and $\eta = E_c/k_B T$. These measurements are critical for validating the STA trajectory, which shows superior performance compared with the non-STA approach in preserving the initial energy distribution.

Experimental results are shown in Fig. 1(c), where the atomic state distributions are measured after transportation, by adjusting the trap depth according to the adiabatic trap lowering sequence adapted from Refs. [15,28]. The experimental data are shown for before (black crosses) and after transportation

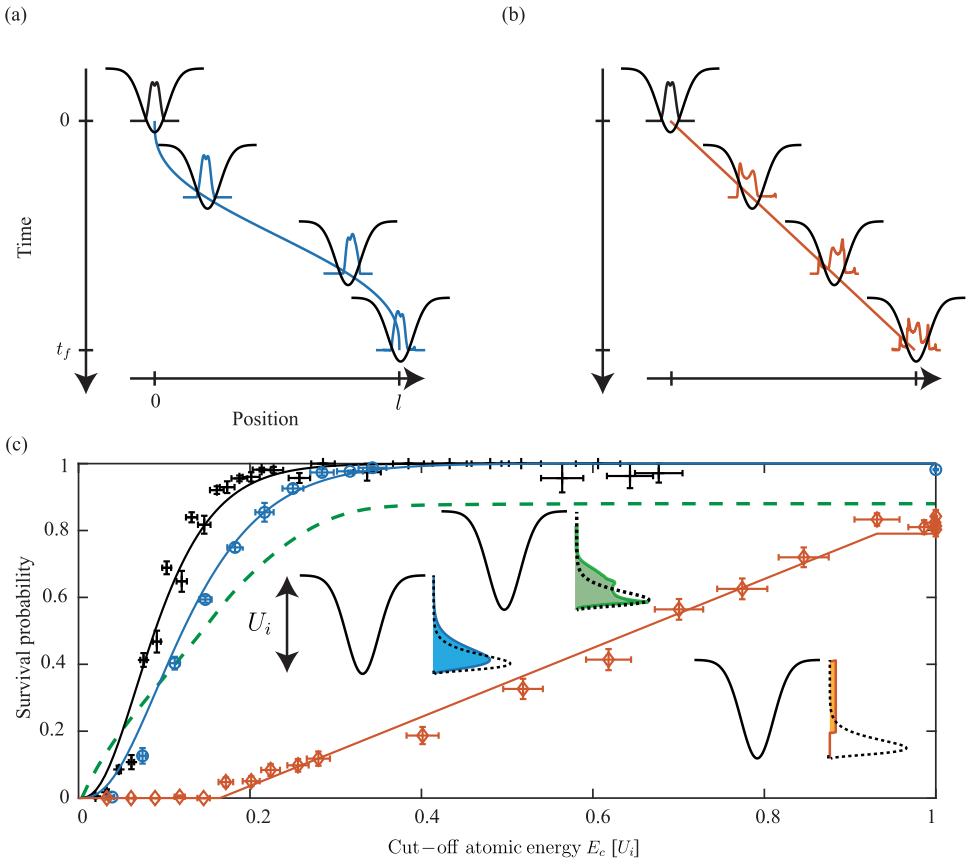

Fig. 1. STA-based atom transport trajectory compared with non-STA trajectories. (a),(b) Schematic of transport trajectories of the optical tweezer with transportation duration $t_f = 58.5$ μs and distance $l = 12.6$ μs: (a) the STA-based solution in Eqs. (5) and (6); (b) a corresponding constant velocity (CV), non-STA trajectory. The black lines represent the optical potential of harmonically approximated optical tweezers. The shape of the atomic wave packet is well maintained through the STA path (blue), but it is deformed along the non-STA path (orange). (c) The survival probabilities of atoms after the transportation, measured as a function of the cutoff atomic energy E_c by varying the minimum trap depth $U_{\min}$ in adiabatic trap lowering [15,28]. The black cross markers (blue circle markers, orange diamond markers) represent the survival probability after staying at the initial position (STA transportation, non-STA CV transportation) varying the cutoff atomic energy E_c in unit of initial trap depth ($U_i = 0.8$ mK). In addition, the green dashed line is the numerically calculated atomic distribution after transportation along the constant jerk trajectory ($\tilde{x} = 3\tilde{t}^2 - 2\tilde{t}^3$). The probability density distributions of atoms are correspondingly shown in the inset figures, with respect to the initial trap potential U_i.

(STA with blue circles and non-STA CV with orange diamonds). The black and blue solid line represent the result of fitting the experimental data for before and after the STA transportation to the cumulative probability distribution function of the Maxwell–Boltzmann distribution, as Eq. (9). In the left-hand inset, the probability density distribution of atomic energy after STA transportation is shown by the blue solid line, compared to the black dashed line for no transportation. For an initial atom temperature of 27(3) μK (black dashed line in the inset), the final atom temperature (blue solid line) of 36(4) μK after STA transportation is measured, demonstrating that STA transportation effectively preserves the atomic energy distribution according to the Maxwell–Boltzmann distribution. In contrast, when the atom undergoes constant velocity movement along the non-STA CV path, it deviates from the Maxwell–Boltzmann distribution. Instead, the cumulative probability distribution (orange diamonds) closely follows a piecewise linear function, $P(x = E_c/U_i) = 0\ (0<x<0.165),\ 1.03x - 0.17\ (0.165<x<0.931),\ 0.79\ (0.931<x<1)$, in agreement with expectations that the energy is distributed nearly uniformly among $|n\rangle$ states, where the average energy of the atom is $6.0(2) \times 10^{-27}$ J, which is equivalent to the mean energy of an atom at 0.29(1) mK that follows a Maxwell–Boltzmann distribution ($\bar{E} = 3k_BT/2$). The probability density distribution of atomic energy after non-STA CV transportation, shown by the orange solid line in the right-hand inset figure, reveals a significantly distorted, non-thermal energy distribution, suggesting substantial vibrational heating. Transport success probabilities are measured at $P = 0.98(1)$ for the STA trajectory and 0.80(2) for the non-STA CV trajectory. The observed differences in atomic energy distributions and success probabilities indicate that the STA-based trajectory successfully transports the atom while preserving its initial states, whereas the non-STA CV approach falls into the diabatic transport condition. In comparison, we also present numerical simulation of a corresponding constant jerk (CJ) trajectory [green dashed line in Fig. 1(c)]. This adiabatic protocol produces the final energy distribution that deviates from the Maxwell–Boltzmann distribution, with an average atomic energy of 8.4×10^{-28} J and success probability of 0.93.

4. OPTICAL TWEEZER MODELS FOR EFFECTIVE SPEED LIMITS

In the second experiment, we investigate the conditions for successful STA-based transport to obtain an effective speed limit of STA-based atom transport. Transport failure occurs when the atom escapes the tweezer, a scenario not accounted for in STA theory [14] that assumes an infinite harmonic trap. However, the optical tweezer has a finite trap potential and its distribution follows a Gaussian function rather than a harmonic one. To evaluate the effects of these discrepancies, we employ three different models of the optical tweezer, as depicted in Fig. 2(a), and correlate these findings with experimental results shown in Fig. 2(b).

We first consider an idealized truncated harmonic trap, denoted by Model I in Fig. 2(a), where a transportation failure occurs when the maximum displacement $\xi(t) = x_o(t) - x(t)$ exceeds the trap width d within the time interval $0<t<t_f$, where the atomic trajectory and optical tweezer position are governed by Eqs. (5) and (6), respectively. Consequently, allowed STA trajectories are confined by

$$l_1 < \frac{\sqrt{3}}{5}\frac{U_0}{md}t_f^2, \tag{10}$$

of which the boundary is illustrated with the white dashed line in Fig. 2(a). In the context of atomic state, this can be defined as the condition that the maximal energy state of the atom during STA transport will not exceed the trap energy level ($\Delta n \times \hbar\omega_0 < U_0$; see the Appendix for details). So, the effective transportation speed, obtained from the boundary condition in Fig. 2(a), is constrained by $\bar{v}_1 < 0.34 \times a_{\max} t$, where $a_{\max} = U_0/md$ [19,20] is the maximal inertial acceleration. However, in real optical tweezer systems, Gaussian-distributed potential traps are wider

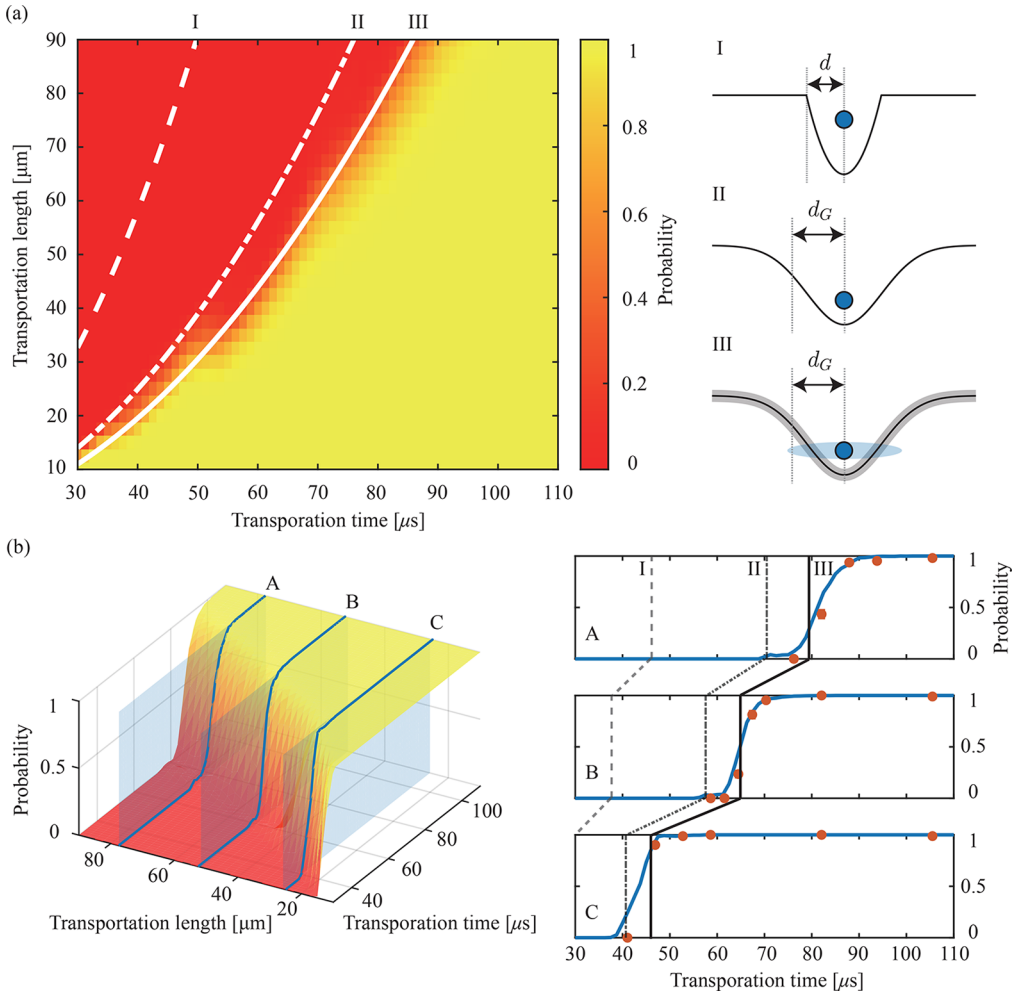

Fig. 2. Success probability $P(t_f, l)$ of STA-based transportation as a function of transportation distance l and duration t_f. (a) Success probability within three different trap models: I (a truncated harmonic trap); II (a Gaussian distributed trap); and III (a Gaussian distributed trap with atomic and trap fluctuations). The background color contours represent the success probability of Model III and the white dashed line (dash–dotted line, and solid line) denotes the boundary condition where atoms escape the optical tweezer for Model I (II, and III). (b) Experimental results of STA-based transportation. The experiments are categorized into three different groups, labeled A, B, and C, whose transportation distances are, respectively, 77.5(3), 51.7(3), and 25.2(3) μm. The experimental results are plotted with orange circles for each of the three groups. The black dashed, dash–dotted, and solid vertical lines represent the boundary conditions of Models I, II, and III, respectively. Each boundary was determined by adjusting the effective trap width and verifying its consistency with numerical calculations for each model, in which the effective trap width is calculated from the extremum of the difference between the Gaussian trap and the harmonic trap in Model II and from the experimental noise effects, the atomic temperature and trap power fluctuations, in Model III. The blue solid line is the success probability of Model III, which is consistent with experimental results.

than harmonic traps, as denoted by Model II in Fig. 2(a). The gentler potential gradient in Gaussian traps produces a weaker net force on atoms, leading to larger displacements ξ and a higher likelihood of transport failure along the same STA path. Taking this anharmonicity issue into account, we numerically calculated the atomic trajectory and displacement as ξ_{G}. A Gaussian trap has a local extreme point at the trap radius d_{G}, where the potential falls to $1/e^2$ of its maximum, especially in our system $d_{\mathrm{G}} = 1.0(1)$ μm. As the atom moves beyond d_{G}, the restoring force diminishes rather than increases, preventing the atom from receiving enough force to return to the trap center and allowing it to escape. Thus, in Model II, where we assume the atom escapes the trap if ξ_G exceeds d_G, the boundary condition is represented by the dash–dotted line in Fig. 2(a) and the resulting effective transportation speed limit is approximated as $\bar{v}_{\mathrm{II}}^{\max} \approx 0.429 \times \bar{v}_{\mathrm{I}}^{\max}$.

Model III provides a more realistic trap representation by incorporating Monte Carlo simulations to account for experimental fluctuations, such as variations in atomic velocity, position distributions, and trap depth changes during optical tweezer controls. The Maxwell–Boltzmann distribution describes the spread of atomic positions and velocities as a function of the atom's temperature, with position fluctuation given by $\Delta x = \sqrt{k_B T/m\omega_0^2}$ and velocity fluctuation given by $\Delta v = \sqrt{k_B T/m}$. To simulate these conditions, we randomized the initial positions and velocities of the atoms and repeated this process 200 times. The force exerted on the atom by the optical tweezer was computed in real time based on the atom's initial conditions and the tweezer trajectory. This force was further adjusted to reflect fluctuations in trap depth ($\Delta U \sim 0.15$ mK), caused by laser power fluctuations and AOD efficiency variations during transport. If, in any of the 200 simulations, the atom's displacement from the trap center exceeded the trap radius ($\max(\xi_{\mathrm{G}}) > \mathrm{d_G}$), the event was classified as an atom escape. The success probability $P(t_f, l)$ was then calculated as the ratio of successful transport cases to the total number of trials. The calculated probability of successful transport is shown as the background color in Fig. 2(a), with the boundary for successful transport is approximated by the solid white line, with the effective speed limit for transportation given by $\bar{v}_{\mathrm{III}}^{\max} \approx 0.336 \times \bar{v}_{\mathrm{I}}^{\max}$.

Experimental results are presented in Fig. 2(b) compared with the success probabilities predicted by the three atomic transport models. The experiments were carried out with three transportation distances of $l_{\mathrm{A}} = 77.5(3)$ μm, $l_{\mathrm{B}} = 51.7(3)$ μm, and $l_{\mathrm{C}} = 25.2(3)$ μm, all under the same trap potential condition of $U = 0.8(2)$ mK, illustrating how they vary with different transportation times. The black dashed, dash–dotted, and solid lines represent the boundary conditions for the three models. The blue solid curves show the success probabilities for Model III across different transport times, closely matching the experimental data.

5. GENERAL STA TRAJECTORIES

We now explore the feasibility of generating general STA trajectories, including curved ones. Computing a path with a general shape involves defining specific boundary conditions for the trajectory and solving the relevant equations for each new shape. However, rather than recalculating solutions for each new path, we break down a general trajectory into segments consisting of straight and rotational paths, with finite initial and final velocities, and then concatenate these segments. This approach requires two key validations: first, ensuring that concatenated STA paths preserve the initial atomic state after transport; and second, confirming that the generalized rotational path also maintains the initial state. Our next experiments will therefore test whether combined paths remain valid as STA trajectories for atomic transport.

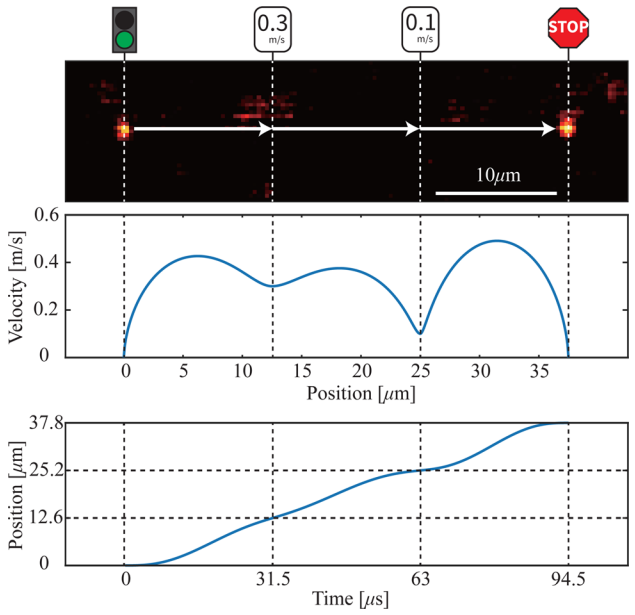

Fig. 3. A concatenation of three STA segments: an atom is guided along three STA segments with the same duration $t_f = 31.5(8)$ μs and distance $l = 12.6(3)$ μm but with different initial and final velocities, (i) $v_i = 0$ m/s and $v_f = 0.3$ m/s, (ii) $v_i = 0.3$ m/s and $v_f = 0.1$ m/s, and (iii) $v_i = 0.1$ m/s, and $v_f = 0$ m/s, respectively. The transportation success probability is measured to $P = 0.99(1)$ and the final temperature $T_f = 15(3)$ μK, when the initial temperature is $T_f = 12(2)$ μK.

Figure 3 presents an atom transport experiment along three concatenated STA paths with different boundary conditions. The atom's velocities are non-zero at the connection points between segments. Following the previous Eq. (3), we calculate three STA linear paths so that each of the segments is of the same travel distance 12.6(3) μm and the same transportation time 31.5(8) μs, while each features different initial and final velocities. This STA transportation is performed outside of the adiabatic transport region, with a transport speed of $\bar{v} = 0.4$ m/s. The experimental result in Fig. 3 shows that a high success probability of $P = 0.99(1)$ is achieved. The temperature is maintained at 15(3) μK, close to the initial temperature of 12(2) μK, confirming that concatenating STA paths can indeed result in a valid STA path. The release-and-recapture method [15] is used to measure the temperatures in general STA trajectory experiments.

Curved STA trajectories are based on Eq. (7), being tested and summarized in Fig. 4. A 90° rotation is illustrated in Fig. 4(a), where $R = 25.2(3)$ μm, $v_i = v_f = 0$ m/s, $t_f = 93.7(8)$ μs, and $\theta_f = \pi/2$. For this case of $v_i = v_f = 0$, the solution is given by $\tilde{\theta}(t) = 10\tilde{t}^3 - 15\tilde{t}^4 + 6\tilde{t}^5$. When we compare the success probability of this STA rotational transport with that of a constant angular velocity optical tweezer, defined by $r(t) = R$ and $\dot{\theta} = \theta_f/t_f$, to see if the atoms maintain their initial state in

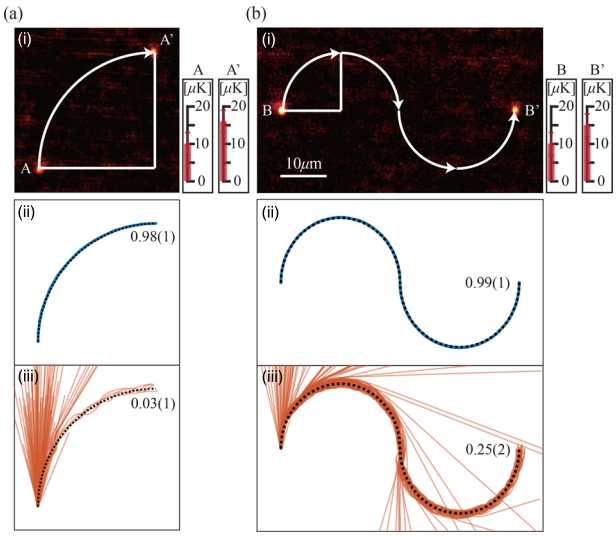

Fig. 4. Curved STA trajectories for atom transport. (a) A 90° circular STA trajectory. (i) An illustrative image of atoms before and after the rotational transportation. As a non-STA transportation, the constant angular velocity trajectory $[r(t) = R, \theta(t) = \theta_f t/t_f]$ is utilized, satisfying the same transportation distance and duration. (ii),(iii) The blue and orange lines represent the atom trajectories during the STA transportation and non-STA transportation, respectively, and the black dotted line represents the trajectory of the trap center for each transportation. (b) An S-shaped STA trajectory. The S-shaped atom trajectory is designed by combining two STA-based semicircular paths, each rotating 180° with the same radius $R = 12.6(3)$ μm within the same duration $t_f = 128.8(8)$ μs but in opposite directions. The final speed of the first semicircle and the initial speed of the second semicircle are $v_{\text{inter}} = 0.3$ m/s. As a non-STA transportation, two of the constant angular velocity trajectories with $r(t) = R, \theta(t) = \theta_f t/t_f$ are combined.

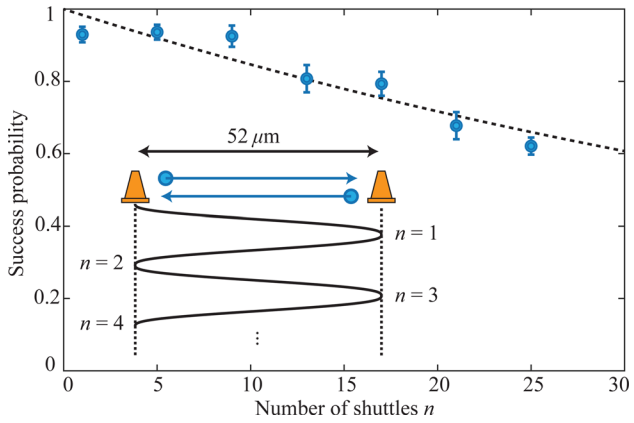

Fig. 5. Atomic shuttle run experiment. An atom is shuttled back and forth between two locations using an STA path with a duration of $t_f = 129.0(8)$ μs over a distance of $l = 51.8(3)$ μm. Success probabilities are measured as a function of one-way run number n for up to $n = 25$ and fitted to $P_s(n) = 0.984(4)^n$.

the diabatic region, an experimental as-designed STA transport results in a high success transport probability of $P = 0.98(1)$ compared with $P = 0.03(1)$ of the non-STA, constant angular velocity trajectory. The temperature is well maintained at 16(3) μK close to the initial temperature of 10(3) μK. An 'S'-shaped transportation path is also implemented by combining two semicircular segments based on the STA-based rotation solution, as illustrated in Fig. 4(b). The semicircular paths rotate 180° in opposite directions with the same radius of $R = 12.6(3)$ μm within duration of $t_f = 128.8(8)$ μs. To maintain continuous motion without reducing speed to zero at the intersection, the final speed of the first semicircle is matched to the initial speed of the second semicircle, i.e., $R\dot{\theta}_1(t_f) = R\dot{\theta}_2(0) = 0.3$ m/s. For comparison, non-STA transport is tested with a constant average angular velocity $\dot{\theta} = \pi/t_f$. Model III simulations show that the STA atom trajectory [Fig. 4(b ii)], is more convergent to the trap center than the non-STA trajectory in Fig. 4(b iii). This is consistent with experimental success probabilities of $P = 0.99(1)$ for STA and $P = 0.25(2)$ for non-STA transport, where the low probability of the non-STA transport can be attributed to atom leakage along the normal direction, caused by the centrifugal force acting on curved paths. The atom's temperature is well maintained in the STA transportation, with the final temperature of 15(3) μK matching the initial temperature of 10(3) μK.

Furthermore, in the context of long-distance atom transport, we have conducted an experiment of repeatedly shuttling an atom between two locations, which we may term "atomic shuttle running". This test estimates the maximum transport distance achievable within the field of view, which is approximately 100 μm squares, limited by our EMCCD (electron multiplying charge-coupled device) imaging device. As illustrated in the inset of Fig. 5, each one-way travel covers a distance of $l = 51.7(3)$ μm, with a runtime of $t_f = 129.0(8)$ μs. Success probabilities $P_s(n)$ are measured for various repetitions up to $n = 25$ and numerically fitted to

$$P_s(n) = 0.984(4)^n, \tag{11}$$

assuming the effect of the gradual temperature increase during the shuttle run is negligible. This result indicates that the STA-based atom trajectory could span over one centimeter with a success probability exceeding $P_s(n = 200) = 3.9\%$. In contrast, when using a constant-velocity trajectory under the same transport conditions, the success probability is significantly lower at $P_s(n = 1) = 0.42(6)$, implying a transport distance of approximately 200 μm with 3.1% success rate—50 times shorter than the STA approach.

6. DISCUSSION AND CONCLUSION

The STA approach offers notable advantages over the CV $(\tilde{x}_{\text{CV}}(t) = \tilde{t}\,)$ and CJ $(\tilde{x}_{\text{CJ}}(t) = 3\tilde{t}^2 - 2\tilde{t}^3$, for example) trajectories [5,37]. This can be deduced based on the energy state changes that the atoms undergo along each transportation path. If the optical tweezer is treated as a quantum harmonic oscillator, the state of the atom is determined by the force acting on it, which corresponds to the magnitude of its acceleration [38]. If we assume that the atom travels a considerable distance in relation to the trap size and focus on the scenario where the transport is successful, we can disregard the discrepancy between the atom's trajectory and the trap's $(\xi_{\max} < d \ll l)$. Under these assumptions, the atom's real-time acceleration is approximated to match that of the trap and we can calculate the maximum distance the atom can successfully travel in a finite depth of the trap, by considering a situation where the maximum energy of the atom is equal to the trap's energy $(\max|\Delta n(t)| \cdot \hbar\omega_0 = U_0)$. Therefore, the maximum transportable distances scale

as

$$l_{\max} = \begin{cases} \sqrt{\dfrac{2U_0}{m}} \times t_f & \text{for CV path,} \\ \dfrac{1}{3\sqrt{3}} \dfrac{U_0}{md} \times t_f^2 & \text{for CJ path,} \\ \dfrac{\sqrt{3}}{5} \dfrac{U_0}{md} \times t_f^2 & \text{for STA path.} \end{cases} \tag{12}$$

While both CJ and STA can achieve a constant average acceleration motion, i.e., $l_{\max} \propto t_f^2$, they differ in the degree of atom heating, which is dependent upon the final state of the atom, Δn, following movement, as approximated for each trajectory as follows:

$$\Delta n \simeq \begin{cases} \dfrac{ml^2}{2\hbar\omega_0} \times t_f^{-2} & \text{for CV,} \\ \dfrac{36ml^2}{\hbar\omega_0^3} \times t_f^{-4} & \text{for CJ,} \\ \dfrac{3600ml^2}{\hbar\omega_0^5} \times t_f^{-6} & \text{for STA.} \end{cases} \tag{13}$$

When the atom travels a maximal distance $l_{\max}$, as defined by Eq. (12) within 100 μs along three different trajectories, the resulting increases in the final state of the atoms are 188, 125, and 13, respectively. It should be noted that, unlike CJ and CV, the maximum state changes or the final state changes in STA differ significantly in magnitude over time. As a result, for the same success probability in STA, the farther and longer the atom travels, the smaller the final temperature change. As an illustration, if atoms traverse for 1 ms, the potential maximum distance for CV, CJ, and STA are 391 μm, 21 mm, and 38 mm, respectively. Notably, the vibrational state changes of the atom diminishes from 13 to 0.1 for STA trajectory alone, in contrast to the other two paths, which have same increases for 100 μs.

Aside from technical limitations, the success of atom transportation is fundamentally constrained by the trap lifetime, τ_{trap}, which defines the maximum duration an optical tweezer can stably hold atoms. In addition, when considering only the intrinsic limitation of the optical tweezer's Gaussian beam profile, as described in Model II, the success limit of STA is given by $l_2 < 0.0743 d\omega_0^2 t_f^2$. The state-of-the-art trap lifetime is currently 6000 s [17], allowing for 60 s of stable atom guidance with a probability over 0.99. Within this time-frame, an atom could theoretically travel a distance of approximately 3.6×10^7 m at a maximum atom velocity of 6.0×10^5 m/s. However, the limitation of the AOD specification [39], especially access time and trap width restrict the possible trap velocity. The access time is inversely proportional to the size of the incident beam on the AOD (in our setup, 0.75 μs with a beam size of 0.5 mm), and the trap width determines the trap resolution, which is 3 μm for a 1 μm Gaussian width. Therefore, the maximum trap velocity is determined as $v_{\max} = 3\ \mu\text{m}/0.75\ \mu\text{s} = 4$ m/s. Therefore, the atom can expectedly travel a distance 293 μm through 138 μs, where the average velocity of transportation is approximately 2.1 m/s. In addition, an additional technical constraint is the size of the camera windows, given the constraints of our current experimental setup, particularly the EMCCD size (approximately 100 μm), the maximum transport speed in our experiments is estimated to be 0.88 m/s over a distance of $l = 77.5(3)$ μm and a duration of $t_f = 87.9(8)$ μs.

In conclusion, this study has demonstrated that the STA method significantly improves the efficiency and range of atomic transport in optical tweezers, making STA particularly suitable for operating dynamic quantum information devices and other applications requiring precise atomic control. Both experimental and simulation results have shown that STA-based trajectories preserve the Maxwell–Boltzmann energy distribution and avoid vibrational wave packet deformations. The versatility of STA is further illustrated by successful applications to complex curved trajectories, such as S-shaped paths, through the concatenation of multiple STA segments and implementation of STA-based rotations, achieving both high success rate and minimal temperature change. Overall, the STA method offers significant advantages in optimizing experimental efficiency by enabling faster and reliable atom transport, extending the feasible transportation distance within practical trap operation times, thereby proving especially valuable for quantum information devices.

APPENDIX A. ATOMIC STATE CHANGE BY TRAJECTORIES

Atomic transport is evaluated from two perspectives: the success of the transport and the suppression of unwanted heating of atoms. Both perspectives can be judged by atomic state changes during the transport process. First, the success of the transport is determined by the maximum vibrational mode of the atom, $\max|\Delta n(t)|$, because if the maximum state reached by the atom during the transport is equal to or higher than the energy depth of the trap, the atom is likely to escape the trap and the transport will fail. In addition, induced atomic heating by transportation means an increase at the final atomic state.

In a quantum oscillator system, the change of atomic state is dependent on the force F, exactly meaning acceleration a [5,38],

$$\Delta n(t) = \frac{m\,|a(\omega_0)|^2}{2\hbar\omega_0}, \tag{A1}$$

where $a(\omega_0)$ is the Fourier component of a at the trap frequency ω_0 for the time parameter τ ($0<\tau<t$). So, based on this equation, we can estimate the state change of the atom and compare the results of moving the atom for three different paths: (i) the CV trajectory ($\tilde{x}(t) = \tilde{t}$); (ii) the CJ trajectory ($\tilde{x}(t) = 3\tilde{t}^2 - 2\tilde{t}^3$); and (iii) the STA trajectory ($\tilde{x}(t) = 10\tilde{t}^3 - 15\tilde{t}^4 + 6\tilde{t}^5$).

For the CV trajectory, there will be acceleration and deceleration periods during which the atom is forced by the difference between the initial and final velocity of the atom and the trap. Since the atom should be accelerated before the atom can leave the trap ($vt<d$; $v = l/t_f$), the time for acceleration and deceleration of the atom is assumed to be $\tau_{\text{acc}} \sim d/v$, and the acceleration of the atom is practically given by

$$a(t) = \begin{cases} \dfrac{v^2}{d}, & (0 \le t \le \tau_{\text{acc}}), \\ 0, & (\tau_{\text{acc}} < t < t_f - \tau_{\text{acc}}), \\ -\dfrac{v^2}{d} & (t_f - \tau_{\text{acc}} \le t \le t_f). \end{cases} \tag{A2}$$

When $\omega_0\tau_{\text{acc}} \ll 1$, the maximal $|a(\omega_0)|^2$ and the average final $|a(\omega_0)|^2$ are both approximately v^2. Therefore, the maximal atomic state change and final atomic state change is same as $\max|\Delta n(t)| = \Delta n = ml^2/2\hbar\omega_0 t_f^2$. For the CJ path, the acceleration of atom is $a(t) = 6l(1 - 2\tilde{t})/t_f^3$. When $\omega_0 t_f > 1$, the maximal $|a(\omega_0)|^2$ is approximately $108l/\omega_0^2 t_f^4$, and the average final

$|a(\omega_0)|^2$ is approximately $72l/\omega_0^2 t_f^4$. As a result, the maximal atomic state change is $\max|\Delta n(t)| = 54ml^2/\hbar\omega_0^3 t_f^4$ and final atomic state change is same as $\Delta n = 36ml^2/\hbar\omega_0^3 t_f^4$. For the STA path, the acceleration of atom is $a(t) = 60l(\tilde{t} - 3\tilde{t}^2 + 2\tilde{t}^3)/t_f^2$. When $\omega_0 t_f > 1$, the maximal $|a(\omega_0)|^2$ is approximately $100l/3\omega_0^2 t_f^4$, and the average final $|a(\omega_0)|^2$ is approximately $7200l^2/\omega_0^4 t_f^6$. As a result, the maximal atomic state change is $\max|\Delta n(t)| \simeq 50ml^2/3\hbar\omega_0^3 t_f^4$ and final atomic state change is same as $\Delta n = 3600ml^2/\hbar\omega_0^5 t_f^6$.

Funding. National Research Foundation of Korea (RS-2024-00340652).

Disclosures. The authors declare no conflicts of interest.

Data availability. Data underlying the results presented in this paper are not publicly available at this time but may be obtained from the authors upon reasonable request.

REFERENCES

1. M. Saffman, T. G. Walker, and K. Mølmer, "Quantum information with Rydberg atoms," Rev. Mod. Phys. **82**, 2313–2363 (2010).
2. A. Browaeys and T. Lahaye, "Many-body physics with individually controlled Rydberg atoms," Nat. Phys. **16**, 132–142 (2020).
3. S. Ebadi, T. T. Wang, H. Levine, *et al.*, "Quantum phases of matter on a 256-atom programmable quantum simulator," Nature **595**, 227–232 (2021).
4. T. M. Graham, Y. Song, J. Scott, *et al.*, "Multi-qubit entanglement and algorithms on a neutral-atom quantum computer," Nature **604**, 457–462 (2022).
5. D. Bluvstein, H. Levine, G. Semeghini, *et al.*, "A quantum processor based on coherent transport of entangled atom arrays," Nature **604**, 451–456 (2022).
6. M. A. Norcia, W. B. Cairncross, K. Barnes, *et al.*, "Midcircuit qubit measurement and rearrangement in a ^{171}Yb atomic array," Phys. Rev. X **13**, 041034 (2023).
7. D. Bluvstein, S. J. Evered, A. A. Geim, *et al.*, "Logical quantum processor based on reconfigurable atom arrays," Nature **626**, 58–65 (2024).
8. K. Kim, M. Kim, J. Park, *et al.*, "Quantum computing dataset of maximum independent set problem on king's lattice of over hundred Rydberg atoms," Sci. Data **11**, 111 (2024).
9. H. J. Manetsch, G. Nomura, E. Bataille, *et al.*, "A tweezer array with 6100 highly coherent atomic qubits," arXiv (2023).
10. M. A. Norcia, H. Kim, W. B. Cairncross, *et al.*, "Iterative assembly of 171Yb atom arrays with cavity-enhanced optical lattices," arXiv (2024).
11. H. R. Lewis and W. B. Riesenfeld, "An exact quantum theory of the time-dependent harmonic oscillator and of a charged particle in a time-dependent electromagnetic field," J. Math. Phys. **10**, 1458–1473 (1969).
12. A. Polkovnikov and V. Gritsev, "Breakdown of the adiabatic limit in low-dimensional gapless systems," Nat. Phys. **4**, 477–481 (2008).
13. D. Guéry-Odelin, A. Ruschhaupt, A. Kiely, *et al.*, "Shortcuts to adiabaticity: concepts, methods, and applications," Rev. Mod. Phys. **91**, 045001 (2019).
14. E. Torrontegui, S. Ibá nez, X. Chen, *et al.*, "Fast atomic transport without vibrational heating," Phys. Rev. A **83**, 013415 (2011).
15. C. Tuchendler, A. M. Lance, A. Browaeys, *et al.*, "Energy distribution and cooling of a single atom in an optical tweezer," Phys. Rev. A **78**, 033425 (2008).
16. S. de Léséleuc, D. Barredo, V. Lienhard, *et al.*, "Analysis of imperfections in the coherent optical excitation of single atoms to Rydberg states," Phys. Rev. A **97**, 053803 (2018).
17. K.-N. Schymik, S. Pancaldi, F. Nogrette, *et al.*, "Single atoms with 6000-second trapping lifetimes in optical-tweezer arrays at cryogenic temperatures," Phys. Rev. Appl. **16**, 034013 (2021).
18. A. Couvert, T. Kawalec, G. Reinaudi, *et al.*, "Optimal transport of ultracold atoms in the non-adiabatic regime," Europhys. Lett. **83**, 13001 (2008).
19. G. T. Hickman and M. Saffman, "Speed, retention loss, and motional heating of atoms in an optical conveyor belt," Phys. Rev. A **101**, 063411 (2020).
20. H. Hwang, A. Byun, J. Park, *et al.*, "Optical tweezers throw and catch single atoms," Optica **10**, 401 (2023).
21. T. Wang, Z. Zhang, L. Xiang, *et al.*, "The experimental realization of high-fidelity 'shortcut-to-adiabaticity' quantum gates in a superconducting Xmon qubit," New J. Phys. **20**, 065003 (2018).
22. B. Juliá-Díaz, T. Zibold, M. K. Oberthaler, *et al.*, "Dynamic generation of spin-squeezed states in bosonic Josephson junctions," Phys. Rev. A **86**, 023615 (2012).
23. P. Kaufmann, T. F. Gloger, D. Kaufmann, *et al.*, "High-fidelity preservation of quantum information during trapped-ion transport," Phys. Rev. Lett. **120**, 010501 (2018).
24. G. Ness, C. Shkedrov, Y. Florshaim, *et al.*, "Realistic shortcuts to adiabaticity in optical transfer," New J. Phys. **20**, 095002 (2018).
25. A. Ashkin, "Acceleration and trapping of particles by radiation pressure," Phys. Rev. Lett. **24**, 156–159 (1970).
26. N. Schlosser, G. Reymond, I. Protsenko, *et al.*, "Sub-Poissonian loading of single atoms in a microscopic dipole trap," Nature **411**, 1024–1027 (2001).
27. R. Grimm, M. Weidemüller, and Y. B. Ovchinnikov, "Optical dipole traps for neutral atoms," Adv. At., Mol., Opt. Phys. **42**, 95–170 (2000).
28. W. Alt, D. Schrader, S. Kuhr, *et al.*, "Single atoms in a standing-wave dipole trap," Phys. Rev. A **71**, 019905 (2003).
29. F. Nogrette, H. Labuhn, S. Ravets, *et al.*, "Single-atom trapping in holographic 2D arrays of microtraps with arbitrary geometries," Phys. Rev. X **4**, 021034 (2014).
30. W. Lee, H. Kim, and J. Ahn, "Three-dimensional rearrangement of single atoms using actively controlled optical microtraps," Opt. Express **24**, 9816 (2016).
31. H. Kim, W. Lee, H.-g. Lee, *et al.*, "In situ single-atom array synthesis using dynamic holographic optical tweezers," Nat. Commun. **7**, 13317 (2016).
32. W. Lee, H. Kim, and J. Ahn, "Defect-free atomic array formation using the Hungarian matching algorithm," Phys. Rev. A **95**, 053424 (2017).
33. D. Barredo, S. de Léséleuc, V. Lienhard, *et al.*, "An atom-by-atom assembler of defect-free arbitrary two-dimensional atomic arrays," Science **354**, 1021–1023 (2016).
34. E. Urban, T. A. Johnson, T. Henage, *et al.*, "Observation of Rydberg blockade between two atoms," Nat. Phys. **5**, 110–114 (2009).
35. A. Gaëtan, Y. Miroshnychenko, T. Wilk, *et al.*, "Observation of collective excitation of two individual atoms in the Rydberg blockade regime," Nat. Phys. **5**, 115–118 (2009).
36. X.-J. Lu, M. Palmero, I. Lizuain, *et al.*, "Fast driving of a particle in two dimensions without final excitation," Entropy **24**, 1694 (2022).
37. K.-N. Schymik, V. Lienhard, D. Barredo, *et al.*, "Enhanced atom-by-atom assembly of arbitrary tweezer arrays," Phys. Rev. A **102**, 063107 (2020).
38. P. Carruthers and M. M. Nieto, "Coherent states and the forced quantum oscillator," Am. J. Phys. **33**, 537–544 (1965).
39. AA Opto-Electronic, "DTSXY-400-800 Specifications,", AA Opto-Electronic Website, *https://aaoptoelectronic.com/ao-devices/high-resolution-deflectors/l*, accessed August 2, 2024.